Metals and Materials International
https://doi.org/10.1007/s12540-023-01579-4

Microstructure and Crystallographic Texture Evolution of β-Solidifying γ-TiAl Alloy During Single- and Multi-track Exposure via Laser Powder Bed Fusion

Sung-Hyun Park[1] · Ozkan Gokcekaya[1,2] · Ryosuke Ozasa[1,2] · Myung-Hoon Oh[3] · Young-Won Kim[4] · Hyoung Seop Kim[5] · Takayoshi Nakano[1,2]

Received: 20 October 2023 / Accepted: 10 November 2023

Abstract
The microstructural evolution and crystallographic texture formation of β-solidifying Ti-44Al-6Nb-1.2Cr alloy were identified under single- and multi-track exposures via laser powder bed fusion (L-PBF) for various process parameters. Under single-track exposure, the microstructure of the melt pool was divided into the band-like α_2 phase in the melt pool boundary and β phase in the melt pool center. Numerical and thermodynamic simulations revealed that the underlying mechanism of phase separation was related to the variation in the cooling rate in the melt pool, whereas microsegregation induced a shift in the solidification path. Meanwhile, the crystallographic texture of the α_2 phase region was identical to that of the substrate owing to the epitaxial growth of the β phase and subsequent α phase nucleation. In contrast, the β phase exhibited a $\pm 45°$ inclined <100> alignment in the melt pool, which was tilted to align along the build direction toward the center of the melt pool corresponding to the simulated thermal gradient direction. Furthermore, the narrow hatch space condition maintained the crystallographic texture to the subsequent scan, forming a continuous band-like α_2 phase with a strong selection. However, the crystallographic texture in a wide hatch space condition manifested a random distribution and constituted a fine mixture of the β and α_2 phases. For the first time, these results will offer an understanding of an anisotropic microstructure control via the L-PBF process and ensure the tailoring of the mechanical properties in the β-solidifying γ-TiAl-based alloys by approaching hatch spacing control.

Keywords γ-TiAl alloy · Microstructural evolution · Crystallographic texture · Laser powder bed fusion

1 Introduction

To improve energy efficiency, the aerospace and automotive industries have consistently shown interest in lightweight structural materials with superior mechanical properties [1]. In particular, intermetallic γ-titanium aluminide (γ-TiAl)-based alloys are attractive candidates to substitute Ni-based superalloys in the temperature range of 650–850 °C owing to their low density, high-temperature strength, and excellent creep resistance [2, 3]. However, intrinsic problems such as poor room-temperature ductility, low high-temperature deformability, and high reactivity with oxygen and nitrogen make satisfying these requirements and extending their industrial applications difficult [4–6].

To overcome these problems and meet the demand for geometrical complexity and accuracy, a powder bed fusion (PBF) process has been proposed for manufacturing γ-TiAl-based alloy parts. However, unique microstructural

✉ Takayoshi Nakano
nakano@mat.eng.osaka-u.ac.jp

1 Division of Materials and Manufacturing Science, Graduate School of Engineering, Osaka University, 2-1, Yamadaoka, Suita, Osaka 565-0871, Japan

2 Anisotropic Design and Additive Manufacturing Research Center, Osaka University, 2-1, Yamadaoka, Suita, Osaka 565-0871, Japan

3 School of Materials Science and Engineering, Kumoh National Institute of Technology (KIT), 61 Daehakro, Gumi, Gyeongbuk 39177, Republic of Korea

4 Gamteck LLC, Dayton, OH 45431, USA

5 Department of Materials Science and Engineering, Pohang University of Science and Technology (POSTECH), Pohang 37673, Republic of Korea

Published online: 19 December 2023

features still exist because each part is fabricated at a very high cooling rate and has a complex thermal history, wherein track-by-track and layer-by-layer processes are combined to form the final product. The solidification rate of the laser PBF (L-PBF) process for γ-TiAl-based alloy is 10^4–10^6 K/s [7], which is an extremely high cooling rate in comparison with the other typical manufacturing processes, such as die casting, metallic mold casting, arc melting, and crucible levitation melting [8–10]. For example, β-solidifying γ-TiAl alloys constituting a large amount of β stabilizer elements such as Nb and Mo enable mechanical properties superior to those of a conventional γ-TiAl alloy (Ti-48Al-2Nb-2Cr, at%) [11]. The phase transformation sequence in β-solidifying γ-TiAl alloys can be represented as $L \rightarrow L+\beta \rightarrow \beta \rightarrow \alpha+\beta \rightarrow \alpha$ in the slow cooling rate condition [12]. However, the equilibrium phase transformation is suppressed in the rapid solidification state; that is, the L-PBF process is linked to the independent formation of unique microstructural features.

The gas atomization process can provide similar information for investigating the microstructural evolution during rapid solidification. The solidification rate has been reported to be 10^3–10^7 K/s, which varies with the atmosphere during the fabrication process [13], and the phase transformation mechanism in the β-solidifying γ-TiAl alloys depends on local deviations in chemical composition, especially those in the Al composition [14]. Similarly, microsegregation characteristics have been observed in an L-PBF single-track study using simulations [15]. Briefly, in a low Al content region, a martensitic phase transformation ($\beta \rightarrow \alpha'$) is preferred. Whereas, increased Al concentration in the liquid phase results in a peritectic solidification reaction ($L+\beta \rightarrow \alpha$), favoring the massive type transformation during further cooling [14]. The massive transformation is frequently observed in a rapid solidification or quenching condition of γ-TiAl-based alloys [16–18].

In contrast, the L-PBF process promotes epitaxial and/or selective grain growth [19–21]. Furthermore, the crystallographic texture control has the potential to control the final α_2/γ lamellar orientation in β-solidifying γ-TiAl alloys [22, 23], which is significantly attributed to the enhancement of the mechanical properties [24–26]. However, as previously mentioned, the massive transformation has a conflicting point regarding the crystallographic orientation relationship between the parent phase and largely transformed child phase, owing to the absence of a specific orientation relationship between the parent and child phases, that is, a lack of orientation is one of the distinct characteristics [27]. Therefore, crystallographic texture control is considered difficult in β-solidified γ-TiAl alloys fabricated via the L-PBF process. However, in the welding process, which can be considered a manufacturing process similar to the L-PBF process, the massive transformation satisfies the specific orientation relationship between parent and child phases in stainless steels [28, 29].

Consequently, this study focused on the microstructural and crystallographic textural evolution in the initial stage of the Ti-44Al-6Nb-1.2Cr alloy to understand the complex layer-by-layer and track-by-track processes during L-PBF. First, the rapidly solidifying microstructure and crystallographic texture development in a single track were investigated. Numerical and thermodynamic simulations were performed to understand microstructural evolution. Meanwhile, multi-tracks utilizing different hatching spaces enabled two different distinct crystallographic orientations, strong selection in the α_2 phase, and random distribution. The obtained results provide a fundamental understanding of microstructural characteristics during the rapid solidification, and they could facilitate the tailoring of the microstructure of β-solidifying γ-TiAl alloy parts fabricated via the L-PBF process.

2 Methodology

2.1 Materials Preparation

The raw powder of β-solidifying γ-TiAl alloy was fabricated using gas atomization (Osaka Titanium Technologies, Japan), and the nominal chemical composition of the powder was determined to be Ti (balance), Al (43.77), Nb (5.96), and Cr (1.22) (at%) through inductively coupled plasma optical emission spectroscopy. As shown in Fig. 1a, the powder is spherical, and the surface exhibits a dendritic morphology. Furthermore, quantitative analysis of the powder size distribution was performed using a laser diffraction-type particle size distribution measuring device (Mastersizer 3000E, Malvern Panalytical, UK). The obtained volume equivalent diameter D_{50} was 36.0 μm, which is within the range of 10–45 μm (Fig. 1b). A high-circularity powder is expected to result in a high part density owing to its good flowability and high powder layer density.

Single- and multi-track specimens were fabricated using L-PBF (EOS M290, EOS, Germany) on a cast material with the same composition as that of the powder. As shown in Fig. 1c, a 60-μm-thick powder bed was piled up on the casting material, and the used laser power, scanning speed, and hatching space were 180 W, 400–1200 mm/s, and 10, 50 μm, respectively. In the case of the multi-track process, a bidirectional (zigzag) scanning strategy was applied.

2.2 Microstructural Characterization and Mechanical Testing

The topography of each track was observed via optical microscopy (OM; BX60, Olympus, Japan). For the

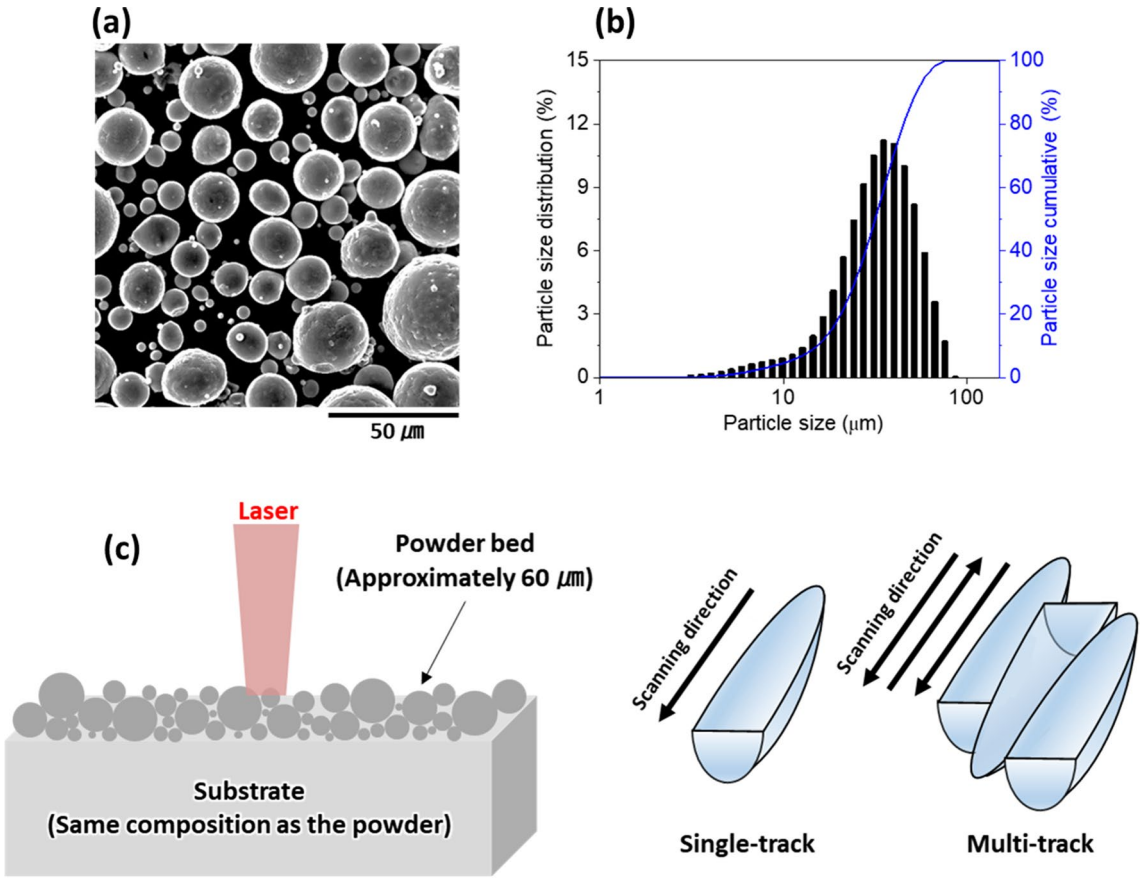

Fig. 1 **a** SEM image, **b** size distribution of the raw powder. **c** Schematic of single-track and multi-track experimental

cross-sectional plane observation, the single-track and multi-track specimens were cut in the transverse direction along the scanning direction and mechanically polished with grinding paper and suspended to the surface of the mirror. The melt pool shape, constituent phase, composition distribution, and crystallographic orientation were determined via field-emission scanning electron microscopy (FE-SEM; JIB-4610F, JEOL, Japan) coupled with energy dispersive X-ray spectroscopy (EDS, X-Max^N, Oxford Instruments, UK) and an electron backscatter diffraction system (EBSD; NordlysMax^3, Oxford Instruments, UK). The mechanical properties were evaluated using a nanoindentation tester (ENT-1100a; ELIONIX, Japan). A Berkovich tip was used, and the maximum indentation load and hold time were set to 4.9 mN and 10 s, respectively.

2.3 Numerical and Thermodynamic Simulations

To further understand the microstructural evolution in the β-solidifying γ-TiAl alloys during the L-PBF process, the thermal diffusion behavior and instantaneous temperature transition were estimated via finite element thermal model simulation (COMSOL Multiphysics 6.1, COMSOL Inc., Sweden), following the methodology introduced in the Ref. [30, 31]. In the simulation, the thermal flux of the laser beam was assumed to satisfy a Gaussian distribution[31, 32]. The energy distribution equation can be expressed as follows:

$$Q = \frac{4AP}{\pi R^2 H}\exp\left(-\frac{2r^2}{R^2}\right)\left[1-\frac{z}{H}\right](0 < z < H) \quad (1)$$

where P is the laser powder; R is the radius of the laser spot; r is the distance between the center of the laser spot and the powder bed surface; A is the rate of laser absorption; H is the laser penetration depth; and z is the depth. In addition, to ensure reliability, the simulated size and shape of the melt pool were compared to the actual size. The physical material properties used in the simulation are listed in Table 1.

The microsegregation was simulated via the Thermo-Calc software with TCTI4 and MOBTI4 database. The Scheil–Gulliver model with the solute trapping algorithm, which was built in the Thermo-Calc software, provided an estimation of the solidification in the material according to non-equilibrium conditions, such as the additive manufacturing process. In general, the solidification behavior is sensitive to the solidification rate, which can be calculated from

Table 1 Material properties and parameters used in the simulations

Properties	Value	Unit
Density	3497–4245	kg/m^3
Latent heat	650	kJ/kg
Thermal conductivity	36.43–54.02	W/(m K)
Specific heat capacity	616–946	J/Kg K
Solidus temperature	1778	K
Liquidus temperature	1823	K

the laser scan speed of a single track by multiplying the angle between the direction of the laser source and the vector normal to the direction of solidification [33]. The calculated solidification rate was approximately 0.56 m/s based on the results obtained from a single track with a laser power of 180 W and scan speed of 800 mm/s.

3 Results and Discussion

3.1 Surface Observations and Melt Pool Geometry of Single Tracks

Figure 2 shows the top surfaces of the single tracks under a fixed scan power and varying scan speed. All process conditions commonly formed cracks in the direction perpendicular to the scanning direction, owing to a large thermal stress below the ductile–brittle transition temperature during rapid solidification [34]. Additionally, as the scan speed increased, the width of the single tracks decreased, and the morphology under moderate scan speed conditions (800 mm/s) showed good continuity and uniformity, whereas low (400 mm/s) or high (1200 mm/s) scan speed conditions induced partial adherence of particles or droplets when the laser power was maintained. The stability of a single track is sensitive to process parameters [35, 36]. The combination of laser power (P) and scan speed (v), the linear energy (P/v), plays a key role in forming consistent and continuous scan tracks, and it should deliver sufficient energy to melt the powders. However, an excessively low scan speed (high energy) generates a melt pool larger than the laser diameter, and the interior of the melt pool is divided into hot and cold regions [37]. The hot region is located under direct laser irradiation, and the existing powder in this section melts completely, whereas the cold region corresponds to the remaining part between the direct laser-irradiated area and melt pool width; therefore, partially melted powders are expected to be attached (400 mm/s). However, a high scan speed (low energy) promotes the instability of the molten track, which causes the splashing of liquid droplets from the surface of the molten track (1200 mm/s) [38, 39].

Figure 3a shows the variation in the melt pool size as a function of the scanning speed under the conditions corresponding to the previous observation. Similarly, the depth (D) and width (W) of the melt pool exhibited a gradually decreasing tendency when the scan speed increased, correlating with the decrease in linear energy. In addition, the melt-pool geometry of the single tracks was classified based on the D/W ratio. With the decreasing scan speed, the melt-pool geometries sequentially changed from keyhole ($R > 1$) to conduction mode (R close to 0.5). Representative cross-sectional images depending on the melt pool geometry are shown in Fig. 3b. The deposition and remelting zones can be distinguished from the cross-section of the melt pool; both regions were observed to be larger under higher linear energy conditions. In terms of attaining the structural integrity of the final products, the accuracy of the part dimensions may be hindered by an overly large deposition zone, whereas an insufficiently small remelting zone leads to weak cohesion between the underlying and adjacent parts, resulting in a lack of fusion. Therefore, to ensure the structural integrity of the final products, the appropriate process parameters were carefully considered.

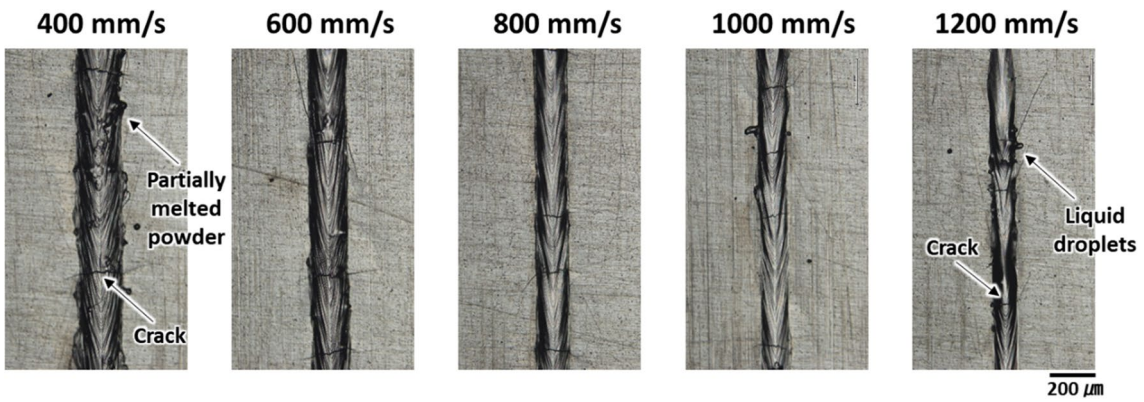

Fig. 2 OM images showing the surface morphology of single tracks with the variation of scan speed

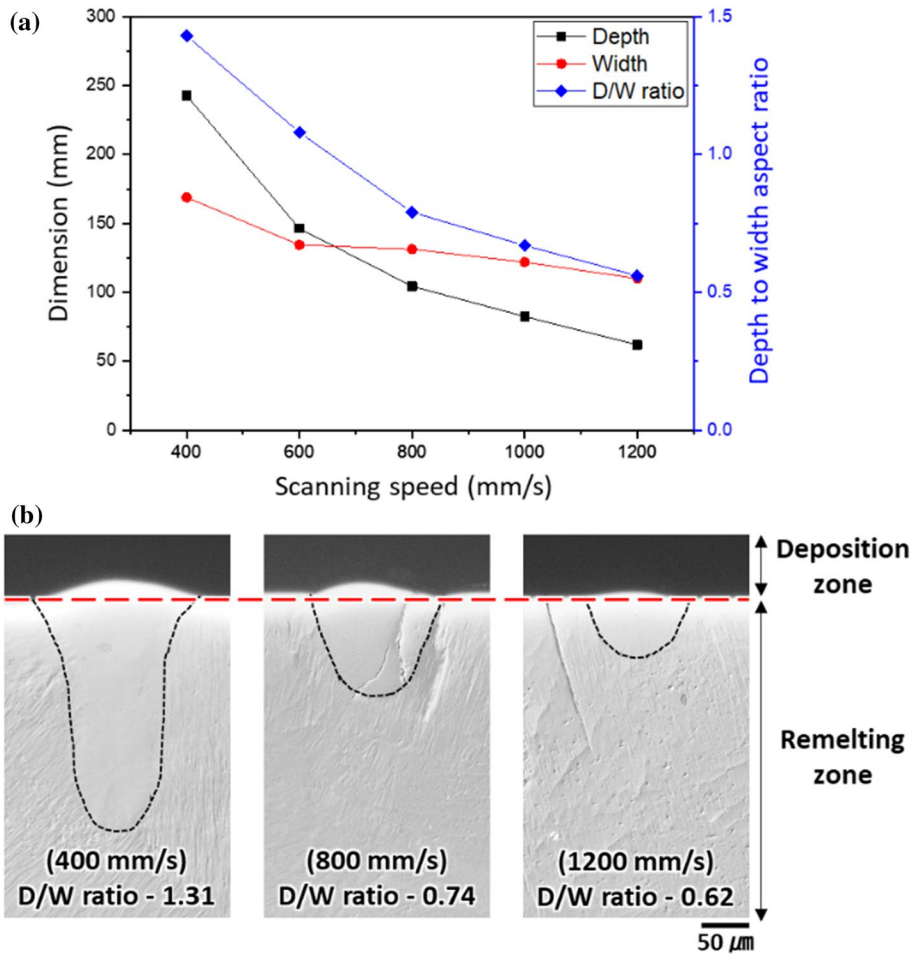

Fig. 3 **a** Effect of scanning speed (linear energy) on the melt pool dimension and **b** shows examples of a cross-section with the typical process conditions

3.2 Microstructural Characterization in the Single Track

For the investigation of the microstructural characteristics, the most stable condition, that is, moderate scan speed (800 mm/s), was selected. Figure 4a and b illustrate the numerically simulated melt pool geometry with the heat flow direction and cross-sectional SEM-BSE image of the melt pool cross-section. Evidently the thermal gradient direction is normal to the melt-pool boundary, and is strongly influenced by the melt-pool shape. Therefore, predominantly $\pm 45°$ inclined solidified microstructure developed in the melt pool boundary, while the direction of solidification gradually becomes closer to the vertical at the melt pool center [40].

Furthermore, the SEM-BSE mode provides a contrast image based on segregation in the chemical composition, where the heavy elements exhibit bright contrast, while the lighter elements exhibit dark contrast. Interestingly, a dark contrast of the substructure with irregular morphology was visible, indicating the aggregation of Al at the melt-pool boundaries (Fig. 4c). Indeed, evaluation of the EDS measurements revealed a discrepancy in the chemical composition between the bright and dark contrast regions, as presented in Table 2. A similar local chemical difference phenomenon was consistently observed in rapidly solidified γ-TiAl alloys[14, 16]. Subsequent investigation of phase distribution utilizing the SEM-EBSD (Fig. 4d) revealed that the substrate (casting) part was predominantly composed of the γ phase, while the inside of the melt pool was divided into two regions: (1) the band-like α_2 phase with the blocky morphology in the melt pool boundary (Dark region) and (2) the β phase in the melt pool center (Bright region). The blocky morphology implies a massive transformation occurred at the melt pool boundary and the thickness of the band-like α_2 phase region was approximately 3–20 μm range. These unusual constituents of the microstructure suggest that microstructural evolution is significantly affected by the cooling rate during solidification.

As demonstrated in the pseudo-phase diagram in Fig. 5, the as-cast β-solidifying γ-TiAl alloys undergo numerous phase transformations under the solidification process, the phase transformation sequence is $L \rightarrow L+\beta \rightarrow \beta \rightarrow \alpha+\beta \rightarrow \alpha$ (Blue line in Fig. 5). Thus, in the substrate (casting) region,

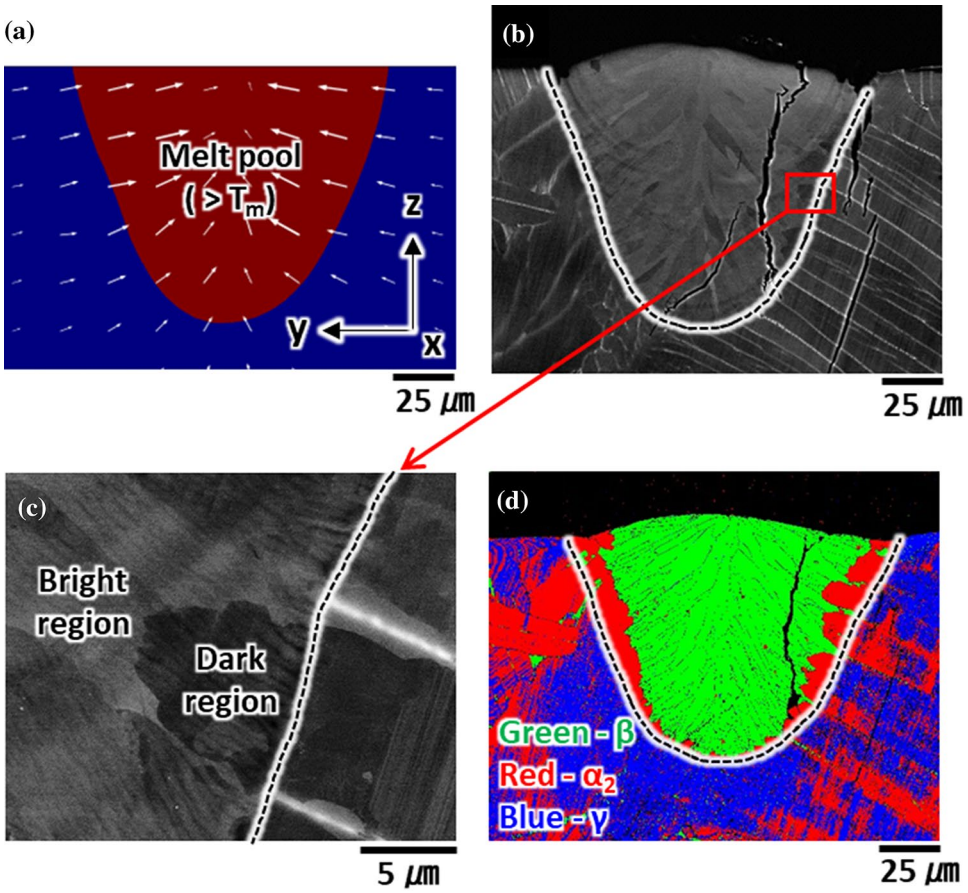

Fig. 4 **a** Results of numerically simulated melt pool geometry in the y–z plane with heat flow directions, **b** SEM-BSE image of a single-track cross-section under 800 mm/s scanning speed, and **c** the highly magnified image at the melt pool boundary region revealing the segregation of composition. **d** SEM-EBSD phase map of the corresponding melt pool

Table 2 Chemical composition of the bright and dark regions indicated in Fig. 4c as obtained utilizing EDS

EDS (at%)	Ti	Al	Nb	Cr
Bright region	49.66 ± 0.10	42.99 ± 0.12	6.05 ± 0.10	1.30 ± 0.03
Dark region	49.26 ± 0.30	43.56 ± 0.31	5.84 ± 0.15	1.34 ± 0.08

the constituted microstructure is represented as the α_2/γ lamellar colonies and segregated β phase [12]. However, the phase transformations in the L-PBF process are quite different. First, the cooling rate variation in a specific region across the melt pool was investigated. Herein, a (Δy, Δz) Cartesian coordinate system is applied to indicate the location in which the cooling rate is measured. The reference point (0, 0) is located at the top center of the melt pool, the Δy is the melt pool width direction from the reference point, and Δz is the variation in the melt pool depth direction, respectively. Commonly, the center of the melt pool shows the highest cooling rate, which gradually decreases with increasing distance from the center of the melt pool (Fig. 6a and b) because the low thermal conductivity of the TiAl alloy induces heat dissipation through the top surface [15]. The decreased cooling rate at the melt pool boundary region provides relatively more time during the solidification, which further induces β to α_2 phase transformation. In contrast, the melt pool center experienced rapid cooling, remaining β phase owing to suppressed phase transformation [41]. In addition, as expected from the high cooling rate, the L-PBF process did not allow sufficient time for the diffusion of the solute. The Scheil-Gulliver solidification simulations predicted microsegregation during rapid solidification. As illustrated in Fig. 6c, the simulation results expected the formation of the β, α_2, and γ phases. Furthermore, the β phase is firstly solidified from the liquid during the solidification, the composition of Al in the liquid gradually increased and reached 49.7% of Al concentration at the initiating stage of the α phase precipitation (Fig. 6d). The different solute diffusivities between the solid and liquid phases led to intensive microsegregation in the cell tip and intercellular regions [15]. Consequently, at the melt pool boundary region, the solidification path is shifted to a higher Al composition, and the massive type of phase transformation is proposed through the single α phase region (Green line in Fig. 5). Meanwhile, the martensitic phase transformation (red line in Fig. 5) occurred at the melt pool center because the region far from the initially nucleated microstructure remained in a perfectly mixed equilibrium liquid state.

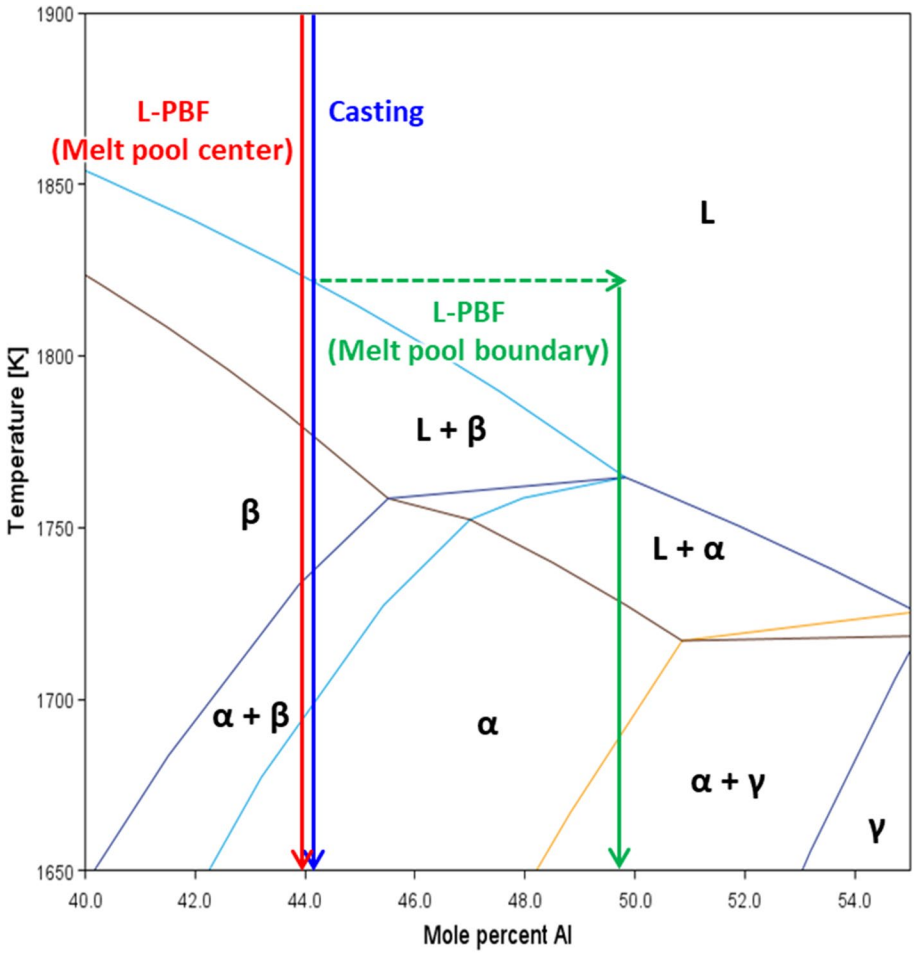

Fig. 5 Pseudo-binary phase diagram of Ti-(40–55)Al-6Nb-1.2Cr alloy calculated with Thermo-Calc software with the schematically illustrated different solidification paths

3.3 Crystallographic Texture Development in the Single Track

The crystallographic texture was investigated based on the microstructural observations. Figure 7a presents the EBSD inverse pole figure (IPF) maps of the corresponding melt pool with previous microstructure observations. In addition, the phase map and IPF maps were obtained at high magnification (Fig. 7b and c). As illustrated in pole figures (PFs) result in the different regions (Fig. 7d), the crystallographic texture of the β phase in the melt pool center (region 1) exhibited ± 45° inclined <100> alignment, which is well matched with the thermal gradient direction represented in the simulated results (Fig. 4a) and generally observed in the cubic based metal alloys [19, 42]. Conversely, the β and α_2 phases at the melt pool boundary interestingly exhibited an identical crystallographic orientation with the substrate (Region 2 and 3). In general, the massive transformation orientation has no specific relationship with the parent and child phases [27]. However, massive epitaxial growth was observed in laser-welded stainless steel when massive growth occurred from a previously existing region of the child phase [28, 29], and the first nucleated massive child grains presented an orientation relationship with the parent phase [18], thus corresponding to the findings of this study.

Figure 8 schematically shows the microstructural evolution and how massive epitaxial grain growth occurred during the L-PBF process based on the results demonstrated in this study. As illustrated in Fig. 8a, when the solidification is initiated from the melt pool boundary, the solidification of the primary β phase results in increasing the concentration of Al composition in the remaining liquid. From the perspective of the crystallographic texture, the β phase, which preferentially grows along the <100> crystal direction, will grow epitaxially with a close alignment to the thermal gradient vector inherited from the seed crystal on the substrate [43, 44]. In addition, the concentration of Al was intensively enriched at the cell tip and intercellular spaces owing to the different diffusivities in the solid and liquid phases, as depicted in Fig. 8b. Afterward, under the continuous cooling state, the α phase nucleated in the interdendritic region following the Burgers orientation relationship, and the crystallographic orientation is arrested during the initial stage of α phase precipitation [29]. Finally, the high

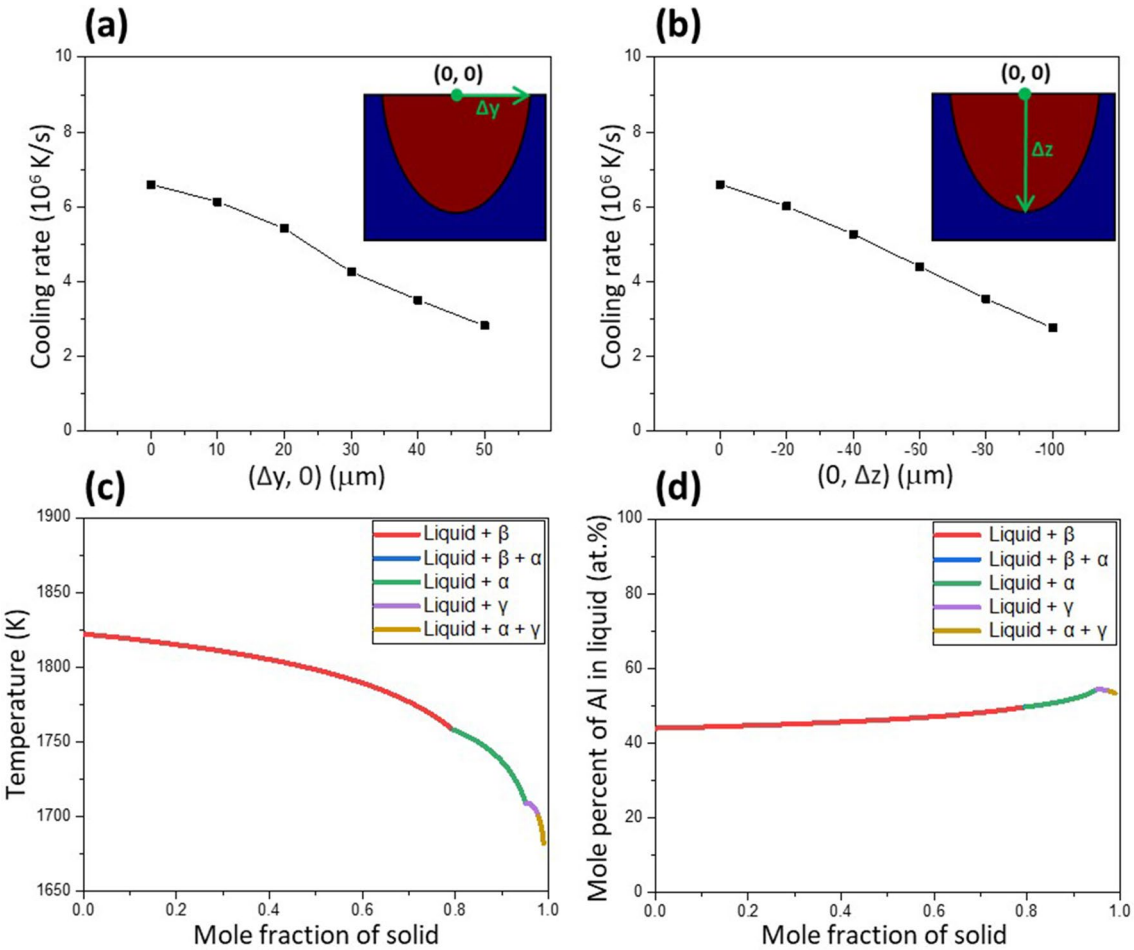

Fig. 6 Variation of the cooling rate in the specific region along the **a** y direction (melt pool depth) and **b** z direction (melt pool width). Scheil-Gulliver simulation of the phase transformation during the solidification process. **c** mole fraction of solid as a function of temperature, and **d** mole fraction of solid as a function of mole percent of Al in liquid

Al concentration induces the α phase transformed at the melt pool boundary toward consuming the primary β phase while crystallographic orientation was maintained. However, martensitic transformation occurred in the melt-pool center region, which experienced a higher cooling rate (Fig. 6a and b) than the melt-pool boundary (Fig. 8c). Moreover, there was no chemical disequilibrium in the melt pool center, and the crystallographic texture varied according to the change in the thermal gradient direction.

3.4 Overlapped Microstructure with the Different Hatch Spacing Condition

In the previous observation of the single-track, the melt pool boundary interestingly consisted of the massively transformed α_2 phase and its crystallographic texture inherited from the substrate through epitaxial growth of β phase and subsequent α phase nucleation following Burger orientation relationship. The thickness of the α_2 phase region approximately ranged between 3 and 20 μm. Thus, to investigate the microstructure continuity in terms of α_2 phase selection with the multi-track study, 10 μm (narrow) and 50 μm (wide) hatch spacing conditions were determined. Firstly, the different hatch spacing conditions showed different microstructural evolution tendencies, as illustrated in Fig. 9. The microstructure under the narrow hatching space condition closely resembled the previous single-track microstructure, which consisted of massive α_2 phase at the melt pool boundary. Whereas, the wide hatching space condition formed the mixture of the fine massive α_2 phase and acicular region, owing to the fluctuation of the temperature resulting from the adjacent scan track. In addition, Fig. 10 shows the EBSD phase, IPF maps, and PFs obtained using different hatching spaces under the same process conditions. As inferred from the microstructure observation, the phase of the melt pool consisted of the massive α_2 phase in the melt pool boundary and the martensitic formed β phase region in the melt pool center (Fig. 10a and d). Furthermore, note that

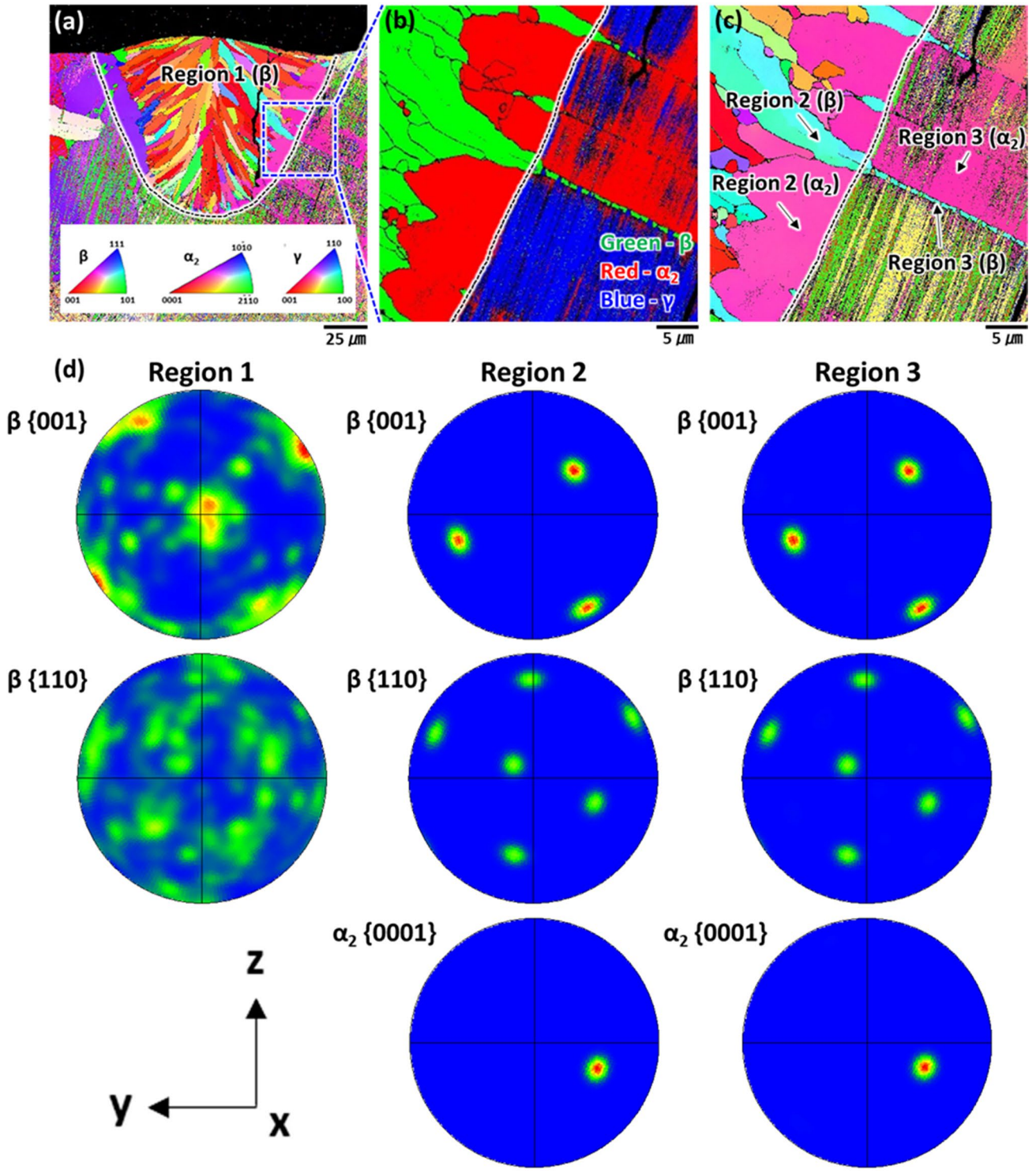

Fig. 7 **a** SEM-EBSD IPF map corresponding to Fig. 4d, and high magnification of **b** phase map and **c** IPF map at the melt pool boundary, respectively. **d** PFs for the β and α_2 phases were obtained from the different regions

the inherited crystallographic orientation from the substrate is continuously maintained in the narrow hatching condition presenting the same α_2 crystallographic orientations with the neighboring regions (Fig. 10b and c). Conversely, although the identical crystallographic texture was observed in the initial stage of the scan track (region 1, 2), the random crystallographic texture was developed (region 3,4) in the wide hatching space condition as the multi-track progressed

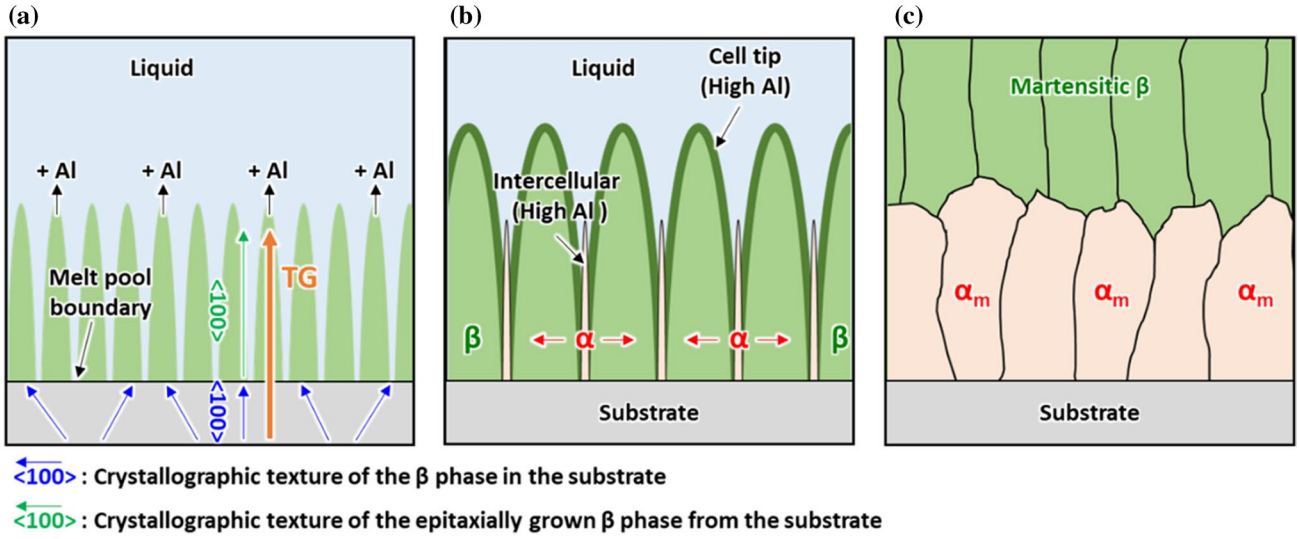

Fig. 8 Schematics of the microstructure evolution process demonstrated in this study. please see the text for further details

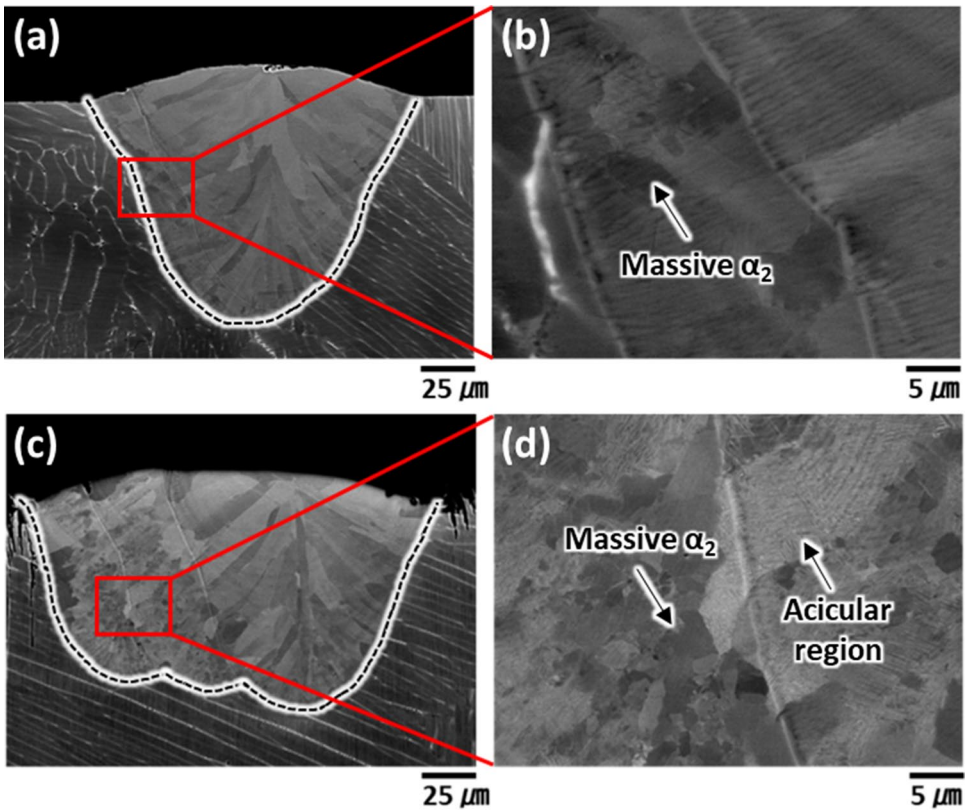

Fig. 9 **a**, **c** SEM-BSE image of the multi-track cross-section under the narrow and wide hatch spacing condition and **b**, **d** enlarged image of the overlapped melt pool regions, respectively

(Fig. 10e and f), indicating difficulty to achieve epitaxial growth of α_2 phase between the scan tracks with wide hatching space.

Figure 11 schematically illustrates the microstructural development for narrow and wide hatch spacings. The previously observed crystallographic texture in the single-track melt pool represented the single crystalline at the melt pool boundary, which inherited the crystallographic texture from the substrate, and the crystallographic texture in the center of the melt pool continuously rotated along the thermal gradient direction changing the grain orientation, thus resulting polycrystal-like β phase region. However, the narrow hatching condition which was smaller than the epitaxially massive grown α_2 phase region reaching 20 μm as presented in the

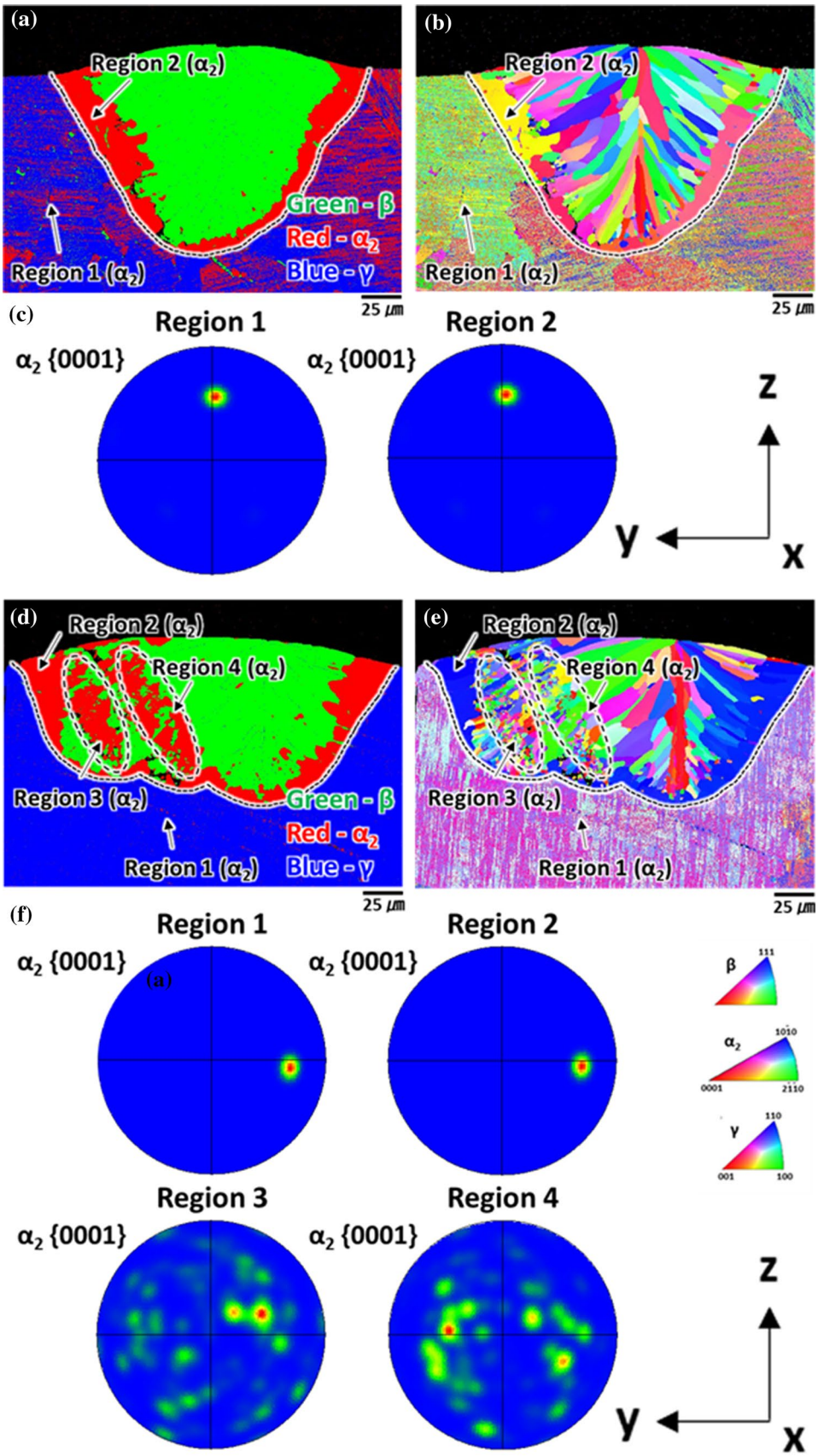

Fig. 10 **a**, **d** SEM-EBSD phase, **b**, **e** IPF map, **c**, **f** PFs of **a**, **b**, and **c** narrow hatching space condition, and **d**, **e**, **f** wide hatching space conditions, respectively

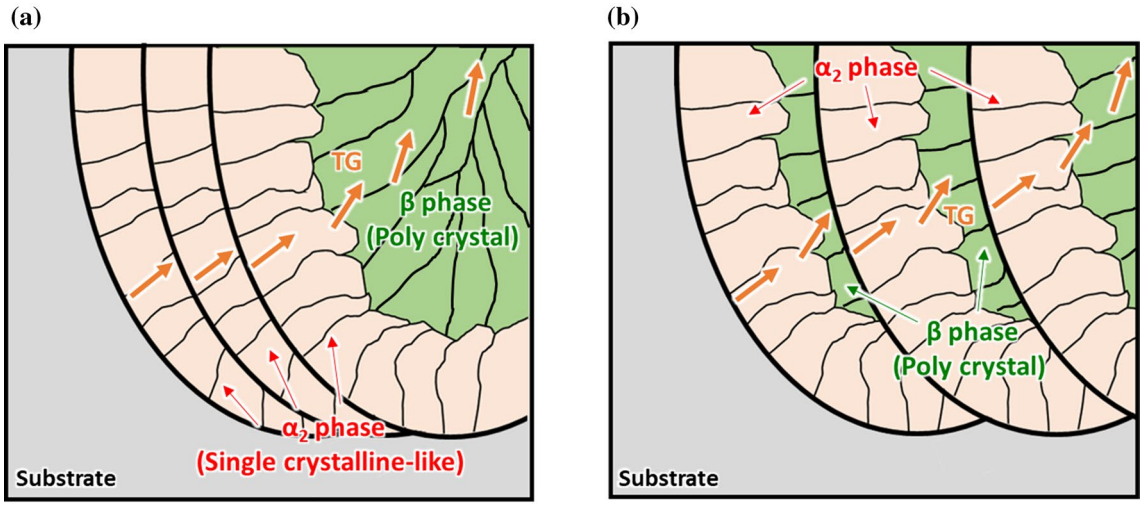

Fig. 11 Schematic of the microstructure formation with **a** the narrow hatching space and **b** wide hatching space conditions, respectively

single melt pool was successful in providing the specifically oriented crystallographic texture to the adjacent track. Such inheritance of the crystallographic texture is well maintained at least within the massive α_2 phase region. However, in the wider hatching space condition, the differently oriented β phase grains act as seed crystals, resulting in the grains being competitively nucleated affected by the thermal cycling from the adjacent scan track and growing in different orientations. Therefore, inheriting a specific crystallographic orientation for the next scan track is difficult, which prevails in random crystallographic textures.

Finally, mechanical properties were evaluated using a nanohardness tester. As shown in Fig. 12a and b, the hardness of the melt pool center (β phase) is commonly higher than the substrate (α_2/γ). In the β-solidifying γ-TiAl alloy, the different crystal structures of each phase are attributed to differences in the hardness, the values are increased in the order of γ, α_2, α_2/γ, and β [45, 46]. Thus, the enhancement of the hardness in the melt pool center region compared to the substrate can be explained by the phase constitution, and the large residual stress resulting from the rapid solidification of the L-PBF process also increases the hardness[47]. Meanwhile, the hardness in the mixture of the fine massive α_2 phase and acicular was significantly higher in the wide hatching space condition. This can be attributed to the influence of small grain size and randomly distributed crystallographic texture. The representative indentation load-depth curves measured at the overlapped microstructure region and the previously observed microstructural characteristics with different hatching space conditions resulted in a distinct hardness behavior (Fig. 12c). Namely, the single crystalline-like α_2 massive region in the narrow hatching space condition low strength, and high ductility can be estimated from the lowest hardness and high penetration depth, respectively.

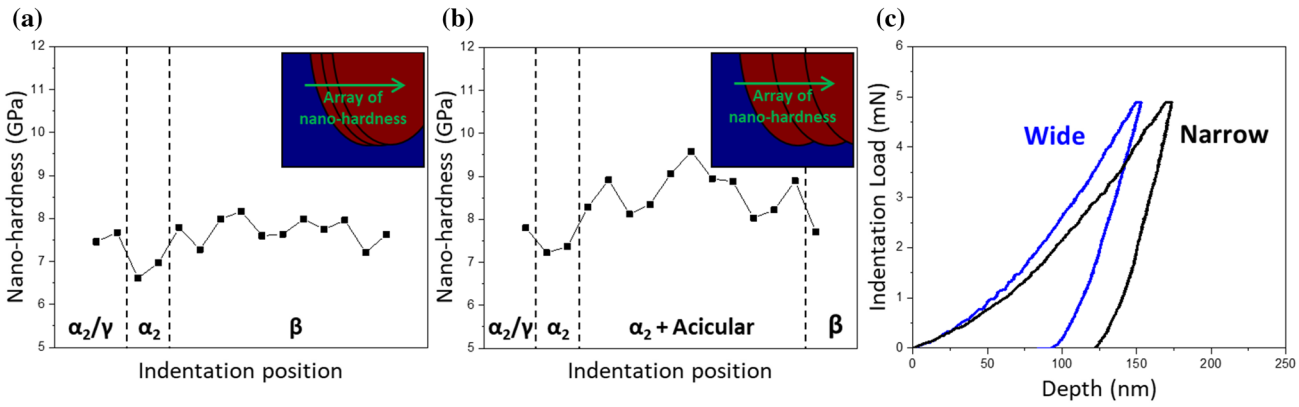

Fig. 12 Array of nano-hardness from the substrate across a melt pool at a different position under the **a** narrow hatching space and **b** wide hatching space condition, respectively. **c** The indentation-load and depth curves for overlapped microstructure regions

However, wide hatching space conditions may result in high strength and low ductility. Consequently, this study demonstrated that appropriate hatching space conditions should be considered to satisfaction of specific mechanical requirements in the β-solidifying γ-TiAl alloys for the first time in the literature. Moreover, a detailed study of the microstructural evolution and its correlation with the mechanical properties of the bulk specimen is in progress and will be reported elsewhere.

4 Conclusions

The single- and multi-tracks Ti-44Al-6Nb-1.2Cr alloy were deposited via the L-PBF process under various process parameters. In addition, the microstructural and crystallographic texture evolution were investigated using numerical and thermodynamic simulations. The following conclusions were drawn:

1. The stability of the tracks and melt-pool geometry changed depending on the linear energy. Partially melted powders were attached to the surface under high-energy conditions, and keyhole-shaped melt pools were observed. The melt pool geometry gradually changed into the conduction mode under low-energy conditions.
2. The microstructure in the melt pool was divided into band-like massive α_2 phase in the melt pool boundary and the β phase in the center of the melt pool because of the variation of cooling rates inside of melt pool and local deviation of chemical composition when the primary β phase was solidified.
3. The crystallographic texture of massive α_2 phases at the melt pool boundary inherited an identical crystallographic orientation with the substrate, resulting from epitaxial growth of the β phase and subsequent phase transformation. Conversely, the β phase in the center exhibited $\pm 45^\circ$ inclined <100> alignment, which is matched with the thermal gradient direction.
4. In the multi-track, the narrow hatch space condition successfully maintained its crystallographic texture to the subsequent scan track through the continuous band-like α_2 phase with a strong selection. However, the crystallographic texture in a wide hatch space condition manifested a randomly distributed α_2 phase owing to the differently oriented β phase grains inducing the grains to be competitively nucleated and growing in different orientations.

Acknowledgements This work was supported by a Grants-in-Aid for Scientific Research (grant number JP23H00235) from the Japan Society for the Promotion of Science (JSPS) and CREST-Nanomechanics: Elucidation of macroscale mechanical properties based on understanding nanoscale dynamics of innovative mechanical materials (Grant Number: JPMJCR2194) from the Japan Science and Technology Agency (JST).

Funding Open access funding provided by Osaka University.

Declarations

Conflict of interest The authors declare that they have no known competing financial interests or personal relationships that could have appeared to influence the work reported in this paper.

References

1. J.C. Williams, E.A. Starke, Progress in structural materials for aerospace systems. Acta Mater. **51**, 5775–5799 (2003). https://doi.org/10.1016/j.actamat.2003.08.023
2. Y.-W. Kim, Intermetallic alloys based on gamma titanium aluminide. JOM **41**, 24–30 (1989). https://doi.org/10.1007/BF03220267
3. Y.-W. Kim, S.-L. Kim, Advances in gammalloy materials–processes–application technology: successes, dilemmas, and future. JOM **70**, 553–560 (2018). https://doi.org/10.1007/s11837-018-2747-x
4. H. Clemens, S. Mayer, Design, processing, microstructure, properties, and applications of advanced intermetallic TiAl alloys. Adv. Eng. Mater. **15**, 191–215 (2013). https://doi.org/10.1002/adem.201200231
5. C. Yuan, X. Cheng, G.S. Holt, D. Shevchenko, P.A. Withey, Investment casting of Ti–46Al–8Nb–1B alloy using moulds with CaO-stabilized zirconia face coat at various mould pre-heat temperatures. Ceram. Int. **41**, 4129–4139 (2015). https://doi.org/10.1016/j.ceramint.2014.11.109
6. S. Lee, M.-S. Shin, Y.-J. Kim, Development of non-reactive mold for investment casting of Ti-48Al-2Cr-2Nb alloys. Metall. Mater. Trans. B **51**, 861–869 (2020). https://doi.org/10.1007/s11663-020-01780-5
7. P. Gao, W. Huang, H. Yang, G. Jing, Q. Liu, G. Wang, Z. Wang, X. Zeng, Cracking behavior and control of β-solidifying Ti-40Al-9V-0.5Y alloy produced by selective laser melting. J. Mater. Sci. Technol. **39**, 144–154 (2020). https://doi.org/10.1016/j.jmst.2019.08.026
8. E. Lee, B. Mishra, Effect of solidification cooling rate on mechanical properties and microstructure of Al-Si-Mn-Mg Alloy. Mater. Trans. **58**, 1624–1627 (2017). https://doi.org/10.2320/matertrans.M2017170
9. T. Nagase, M. Takemura, M. Matsumuro, T. Maruyama, Solidification microstructure of AlCoCrFeNi2.1 eutectic high entropy alloy ingots. Mater. Trans. **59**, 255–264 (2018). https://doi.org/10.2320/matertrans.F-M2017851

10. T. Nagase, K. Mizuuchi, T. Nakano, Solidification microstructures of the ingots obtained by arc melting and cold crucible levitation melting in TiNbTaZr medium-entropy alloy and TiNbTaZrX (X = V, Mo, W) high-entropy alloys. Entropy **21**, 483 (2019). https://doi.org/10.3390/e21050483
11. B.P. Bewlay, S. Nag, A. Suzuki, M.J. Weimer, TiAl alloys in commercial aircraft engines. Mater. High Temp. **33**, 549–559 (2016). https://doi.org/10.1080/09603409.2016.1183068
12. X. Ding, L. Zhang, J. He, F. Zhang, X. Feng, H. Nan, J. Lin, Y.W. Kim, As-cast microstructure characteristics dependent on solidification mode in TiAl-Nb alloys. J. Alloys Compd. **809**, 151862 (2019). https://doi.org/10.1016/j.jallcom.2019.151862
13. R. Gerling, H. Clemens, F.P. Schimansky, Powder metallurgical processing of intermetallic gamma titanium aluminides. Adv. Eng. Mater. **6**, 23–38 (2004). https://doi.org/10.1002/adem.200310559
14. M. Kastenhuber, T. Klein, B. Rashkova, I. Weißensteiner, H. Clemens, S. Mayer, Phase transformations in a β-solidifying γ-TiAl based alloy during rapid solidification. Intermetallics **91**, 100–109 (2017). https://doi.org/10.1016/j.intermet.2017.08.017
15. X. Zhang, B. Mao, L. Mushongera, J. Kundin, Y. Liao, Laser powder bed fusion of titanium aluminides: an investigation on site-specific microstructure evolution mechanism. Mater. Des. **201**, 109501 (2021). https://doi.org/10.1016/j.matdes.2021.109501
16. C. Kenel, C. Leinenbach, Influence of Nb and Mo on microstructure formation of rapidly solidified ternary Ti-Al-(Nb, Mo) alloys. Intermetallics **69**, 82–89 (2016). https://doi.org/10.1016/j.intermet.2015.10.018
17. D. Hu, H. Jiang, Martensite in a TiAl alloy quenched from beta phase field. Intermetallics **56**, 87–95 (2015). https://doi.org/10.1016/j.intermet.2014.09.007
18. S.R. Dey, E. Bouzy, A. Hazotte, EBSD characterisation of massive γ nucleation and growth in a TiAl-based alloy. Intermetallics **14**, 444–449 (2006). https://doi.org/10.1016/j.intermet.2005.08.010
19. T. Ishimoto, K. Hagihara, K. Hisamoto, S.-H. Sun, T. Nakano, Crystallographic texture control of beta-type Ti–15Mo–5Zr–3Al alloy by selective laser melting for the development of novel implants with a biocompatible low Young's modulus. Scr. Mater. **132**, 34–38 (2017). https://doi.org/10.1016/j.scriptamat.2016.12.038
20. T. Ishimoto, K. Hagihara, K. Hisamoto, T. Nakano, Stability of crystallographic texture in laser powder bed fusion: understanding the competition of crystal growth using a single crystalline seed. Addit. Manuf. **43**, 102004 (2021). https://doi.org/10.1016/j.addma.2021.102004
21. M. Simonelli, Y.Y. Tse, C. Tuck, On the texture formation of selective laser melted Ti-6Al-4V. Metall. Mater. Trans. A **45**, 2863–2872 (2014). https://doi.org/10.1007/s11661-014-2218-0
22. I.S. Jung, H.S. Jang, M.H. Oh, J.H. Lee, D.M. Wee, Microstructure control of TiAl alloys containing β stabilizers by directional solidification. Mater. Sci. Eng. A **329–331**, 13–18 (2002). https://doi.org/10.1016/S0921-5093(01)01494-0
23. G. Chen, Y. Peng, G. Zheng, Z. Qi, M. Wang, H. Yu, C. Dong, C.T. Liu, Polysynthetic twinned TiAl single crystals for high-temperature applications. Nat. Mater. **15**, 876–881 (2016). https://doi.org/10.1038/nmat4677
24. H. Inui, M.H. Oh, A. Nakamura, M. Yamaguchi, Room-temperature tensile deformation of polysynthetically twinned (PST) crystals of TiAl. Acta Metall. Mater. **40**, 3095–3104 (1992). https://doi.org/10.1016/0956-7151(92)90472-Q
25. T. Nakano, T. Kawanaka, H.Y. Yasuda, Y. Umakoshi, Effect of lamellar structure on fracture behavior of TiAl polysynthetically twinned crystals. Mater. Sci. Eng. A **194**, 43–51 (1995). https://doi.org/10.1016/0921-5093(94)09658-9
26. Y. Umakoshi, T. Nakano, Plastic behaviour of TiAl crystals containing a single set of lamellae at high temperatures. ISIJ Int. **32**, 1339–1347 (1992). https://doi.org/10.2355/isijinternational.32.1339
27. T.B. Massalski, Massive transformations revisited. Metall. Mater. Trans. A **33**, 2277–2283 (2002). https://doi.org/10.1007/s11661-002-0351-7
28. H. Inouetoshlhlko, K.S. Ohkita, T. Tanaka, Effect of soliditication on subsequentferrite-to-austenite massive transformation in an austenitic stainless steel weld metal. ISIJ Int. **35**, 1248–1257 (1995). https://doi.org/10.2355/isijinternational.35.1248
29. M.J. Perricone, J.N. Dupont, T.D. Anderson, C.V. Robino, J.R. Michael, An investigation of the massive transformation from ferrite to austenite in laser-welded Mo-bearing stainless steels. Metall. Mater. Trans. A **42**, 700–716 (2011). https://doi.org/10.1007/s11661-010-0433-x
30. O. Gokcekaya, T. Ishimoto, T. Todo, P. Wang, T. Nakano, Influence of powder characteristics on densification via crystallographic texture formation: pure tungsten prepared by laser powder bed fusion. Addit. Manufact. Lett. **1**, 100016 (2021). https://doi.org/10.1016/j.addlet.2021.100016
31. T. Todo, T. Ishimoto, O. Gokcekaya, J. Oh, T. Nakano, Single crystalline-like crystallographic texture formation of pure tungsten through laser powder bed fusion. Scr. Mater. **206**, 114252 (2022). https://doi.org/10.1016/j.scriptamat.2021.114252
32. A. Takase, T. Ishimoto, N. Morita, N. Ikeo, T. Nakano, Comparison of phase characteristics and residual stresses in ti-6al-4v alloy manufactured by laser powder bed fusion (L-PBF) and electron beam powder bed fusion (EB-PBF) techniques. Crystals **11**, 796 (2021). https://doi.org/10.3390/cryst11070796
33. P. Mohammadpour, H. Yuan, A.B. Phillion, Microstructure evolution of Inconel 625 alloy during single-track Laser Powder Bed Fusion. Addit. Manuf. **55**, 102824 (2022). https://doi.org/10.1016/j.addma.2022.102824
34. S. Lee, J. Kim, J. Choe et al., Understanding crack formation mechanisms of Ti–48Al–2Cr–2Nb single tracks during laser powder bed fusion. Met. Mater. Int. **27**, 78–91 (2021). https://doi.org/10.1007/s12540-020-00770-1
35. N.T. Aboulkhair, I. Maskery, C. Tuck, I. Ashcroft, N.M. Everitt, On the formation of AlSi10Mg single tracks and layers in selective laser melting: microstructure and nano-mechanical properties. J. Mater. Process. Technol. **230**, 88–98 (2016). https://doi.org/10.1016/j.jmatprotec.2015.11.016
36. J.J.S. Dilip, S. Zhang, C. Teng, K. Zeng, C. Robinson, D. Pal, B. Stucker, Influence of processing parameters on the evolution of melt pool, porosity, and microstructures in Ti-6Al-4V alloy parts fabricated by selective laser melting. Prog. Addit. Manuf. **2**, 157–167 (2017). https://doi.org/10.1007/s40964-017-0030-2
37. A. Keshavarzkermani, E. Marzbanrad, R. Esmaeilizadeh, Y. Mahmoodkhani, U. Ali, P.D. Enrique, N.Y. Zhou, A. Bonakdar, E. Toyserkani, An investigation into the effect of process parameters on melt pool geometry, cell spacing, and grain refinement during laser powder bed fusion. Opt. Laser Technol. **116**, 83–91 (2019). https://doi.org/10.1016/j.optlastec.2019.03.012
38. N.T. Aboulkhair, N.M. Everitt, I. Ashcroft, C. Tuck, Reducing porosity in AlSi10Mg parts processed by selective laser melting. Addit. Manuf. **1**, 77–86 (2014). https://doi.org/10.1016/j.addma.2014.08.001
39. B. Zhang, H. Liao, C. Coddet, Effects of processing parameters on properties of selective laser melting Mg-9%Al powder mixture. Mater. Des. **34**, 753–758 (2012). https://doi.org/10.1016/j.matdes.2011.06.061
40. S.-H. Sun, T. Ishimoto, K. Hagihara, Y. Tsutsumi, T. Hanawa, T. Nakano, Excellent mechanical and corrosion properties of austenitic stainless steel with a unique crystallographic lamellar microstructure via selective laser melting. Scr. Mater. **159**, 89–93 (2019). https://doi.org/10.1016/j.scriptamat.2018.09.017

41. K. Li, X. Wang, N. Brodusch, G. Tu, Mitigating cracking in laser powder bed fusion of Ti-48Al-2Cr-2Nb via introducing massive β phase. Mater. Charact. **196**, 112558 (2023). https://doi.org/10.1016/j.matchar.2022.112558
42. S. Hibino, T. Todo, T. Ishimoto, O. Gokcekaya, Y. Koizumi, K. Igashira, T. Nakano, Control of crystallographic texture and mechanical properties of hastelloy-X via laser powder bed fusion. Crystals **11**, 1064 (2021). https://doi.org/10.3390/cryst11091064
43. J. Liu, A.C. To, Quantitative texture prediction of epitaxial columnar grains in additive manufacturing using selective laser melting. Addit. Manuf. **16**, 58–64 (2017). https://doi.org/10.1016/j.addma.2017.05.005
44. L. Thijs, K. Kempen, J.P. Kruth, J. Van Humbeeck, Fine-structured aluminium products with controllable texture by selective laser melting of pre-alloyed AlSi10Mg powder. Acta Mater. **61**, 1809–1819 (2013). https://doi.org/10.1016/j.actamat.2012.11.052
45. M. Schloffer, F. Iqbal, H. Gabrisch, E. Schwaighofer, F.P. Schimansky, S. Mayer, A. Stark, T. Lippmann, M. Göken, F. Pyczak, H. Clemens, Microstructure development and hardness of a powder metallurgical multi phase γ-TiAl based alloy. Intermetallics **22**, 231–240 (2012). https://doi.org/10.1016/j.intermet.2011.11.015
46. H.Z. Niu, Y.Y. Chen, S.L. Xiao, L.J. Xu, Microstructure evolution and mechanical properties of a novel beta γ-TiAl alloy. Intermetallics **31**, 225–231 (2012). https://doi.org/10.1016/j.intermet.2012.07.012
47. M.S. Wang, E.W. Liu, Y.L. Du, T.T. Liu, W.H. Liao, Cracking mechanism and a novel strategy to eliminate cracks in TiAl alloy additively manufactured by selective laser melting. Scr. Mater. **204**, 114151 (2021). https://doi.org/10.1016/j.scriptamat.2021.114151